ACS NANO

www.acsnano.org

ARTICLE

Perovskite Quantum-Dot Photovoltaic Materials beyond the Reach of Thin Films: Full-Range Tuning of A-Site Cation Composition

Abhijit Hazarika,[†] Qian Zhao,[†,‡] E. Ashley Gaulding,[†] Jeffrey A. Christians,[†] Benjia Dou,[†,§] Ashley R. Marshall,[†] Taylor Moot,[†] Joseph J. Berry,[†] Justin C. Johnson,[†] and Joseph M. Luther*,[†]

[†]National Renewable Energy Laboratory, Golden, Colorado 80401, United States
[‡]College of Chemistry, Nankai University, Tianjin 300071, China
[§]Department of Electrical and Computer Engineering, University of Colorado, Boulder, Colorado 80309, United States

S *Supporting Information*

ABSTRACT: **We present a cation-exchange approach for tunable A-site alloys of cesium (Cs^+) and formamidinium (FA^+) lead triiodide perovskite nanocrystals that enables the formation of compositions spanning the complete range of $Cs_{1-x}FA_xPbI_3$, unlike thin-film alloys or the direct synthesis of alloyed perovskite nanocrystals. These materials show bright and finely tunable emissions in the red and near-infrared range between 650 and 800 nm. The activation energy for the miscibility between Cs^+ and FA^+ is measured (~0.65 eV) and is shown to be higher than reported for X-site exchange in lead halide perovskites. We use these alloyed colloidal perovskite quantum dots to fabricate photovoltaic devices. In addition to the expanded compositional range for $Cs_{1-x}FA_xPbI_3$ materials, the quantum-dot solar cells exhibit high open-circuit voltage (V_{OC}) with a lower loss than the thin-film perovskite devices of similar compositions.**

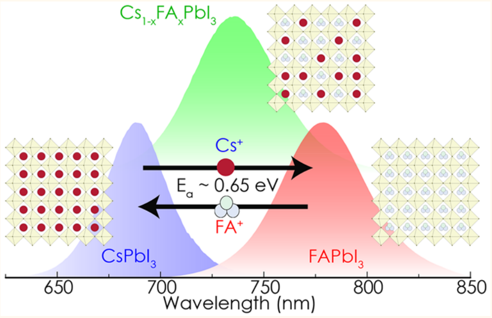

KEYWORDS: *perovskites, quantum dots, cation exchange, solar cells, nanocrystals, A-site alloying, lead halide*

With a record efficiency of ~23.3%,[1] solution-processable lead halide perovskite solar cells are fast approaching the efficiency of commercial wafer-based silicon photovoltaic technology.[2−15] Chemical substitution or alloying on A, B, and X sites allows one to fine-tune various properties of perovskites and, most importantly, to improve their stability.[16−20] Depending on the relative sizes of the ions, ABX_3 materials can adopt different crystallographic structures. The Goldschmidt tolerance factor (GTF), which is expressed as $\mathrm{GTF} = \frac{r_A + r_X}{\sqrt{2}\,(r_B + r_X)}$, where r_i, the effective ionic radius of the individual species, is a geometric formalism often used for simple predictions of the most-likely crystal structure for ABX_3 materials.[21] The general rule of thumb is that a GTF value between 0.9 and 1.0 tends to result in an ideal cubic perovskite structure (α-phase) with undistorted corner-shared octahedra in $APbX_3$ compounds, while GTF values of 0.8−0.9 still lead to perovskite structures but with the tilting of the BX_6 octahedra in either one or multiple dimensions (β and γ phases, respectively).[16,22−25] Slightly above GTF ≈ 1.0, non-perovskite structures tend to form such as the hexagonal δ_h phase with face-shared octahedra, and below 0.8, the edge-sharing orthorhombic δ_o phase is common. Although the GTF fails to explain the formability and stability of perovskites with ideal and tilted corner-shared octahedra,[26] it acts as good starting point to design perovskite materials of interest. For example, A-site alloying allows for the facile tuning of the GTF, which can improve perovskite-phase stability at room temperature.[16] Tuning GTF by A-site alloying allows for some control of the band gap (E_G), a necessity for the development of tandem solar cell architecture; in contrast to methods based on the X-site alloying in which the V_{OC} deficit (defined as the difference between the theoretical limit of open circuit voltage and the observed voltage in real devices) tends to increase with E_G because of halide segregation, A-site alloying can sometimes increase E_G without increasing the V_{OC} deficit.[27,28]

Despite their interest and proven utility, alloys of lead halide perovskites in arbitrary compositions have remained challenging, specifically those alloys in which there exist significantly

Received: July 23, 2018
Accepted: September 20, 2018

DOI: 10.1021/acsnano.8b05555
ACS Nano XXXX, XXX, XXX−XXX

different crystallization temperatures for the pure-component perovskite phases. For example, $FAPbI_3$ deposited from solution is typically annealed at 130 °C,[29] while for $CsPbI_3$, the phase-transition temperature to reach the perovskite phase is around 330 °C.[16] The ideal crystallization temperature for many of the alloys of $Cs_{1-x}FA_xPbI_3$ likely lies between those of these two pure-phase compositions, yet alloy formation is complicated because the organic A-site cations are typically thermally unstable at temperatures above ∼200 °C.[30] The reported synthesis of the perovskite $Cs_{1-x}FA_xPbI_3$ thin films (across the achievable compositions typically with less than 50% Cs) has an annealing temperature of 170 °C, which is the same as that of pure $FAPbI_3$ thin films.[16] However, above this threshold value of Cs incorporation, 170 °C is not adequate to crystallize the perovskite structure and increasing the temperature further results in FA decomposition. Thus, not all compositions of $Cs_{1-x}FA_xPbI_3$ have been realized in the perovskite phase at room temperature from molecular precursors, and it has been demonstrated in a few studies that only compositions with less than 50% Cs can be achieved in the pure α phase (perovskite) without a trace of the undesirable δ phase.[16,19] These reports rely on XRD to detect the phase purity of the alloyed perovskites; however, recently cesium-133 solid-state nuclear magnetic resonance studies reveal that only 15% Cs is actually incorporated in pure perovskite phase, and a higher percentage of Cs incorporation leads to instability of the alloys.[31] In single crystals, even with only 10% Cs, the alloys eventually expel Cs^+ over time.[32] Interestingly, when considering average A-site cation size, all compositions of $Cs_{1-x}FA_xPbI_3$ fall within the ideal region of the GTF for corner-shared perovskite structures, a discrepancy arising because the GTF does not take into account the temperature needed to crystallize the proper phase. Moreover, it is also unclear how the perovskite structure is influenced by strain, an effect overlooked by GTF analysis with average cation size, arising in the lattice due to the mixing of ions like Cs^+ and FA^+, with substantially different ionic radii.

Post-synthetic ion-exchange transformations often allow access to compositions and structures not achievable by direct synthesis,[33−40] but it is not straightforward to use bulk or thin-film metal halide precursors for such ion exchanges because of their solubility in most polar solvents. Colloidal lead halide perovskite nanocrystals (NCs) or quantum dots (QDs) with a "soft" lattice, dynamic surface ligands and a high surface-to-volume ratio are a good platform for ion exchanges. Cation exchanges in chalcogenide and pnictide NCs are well-known and have been demonstrated for a variety of systems like CdE, PbE (E = S, Se, or Te), and InP.[33−38,41] While anion exchanges in traditional chalcogenide NCs are rare, such exchange reactions are known to be more common in perovskite NCs due to fast halide ion movement within the perovskite lattice as well as fast exchange dynamics in solution. For example, reacting $CsPbBr_3$ NCs with alkyl ammonium iodide or chloride precursors can easily and reversibly be transformed to $CsPbI_3$ and $CsPbCl_3$ NCs via ion exchange.[42−46] It has been observed and reported that even simply mixing two types of perovskite NCs in solution (for example, combining $CsPbI_3$ and $CsPbBr_3$ NCs in toluene) can lead to homogeneously alloyed compositions.[42,47] Perovskite NCs are of tremendous importance because of their defect tolerant nature and unique optoelectronic properties like near-unity photoluminescence quantum yield (PLQY) even without epitaxial overcoating with higher-band-gap materials.[48−63] All-inorganic $CsPbI_3$ NCs, unlike their bulk and thin-film counterpart, can be stabilized in the perovskite phase at room temperature in ambient conditions for extended period of time and has been demonstrated as efficient light harvesters in solar cell devices and LEDs.[56,64,65] Apart from the mostly sought-after all-inorganic $CsPbX_3$ NCs, recently colloidal $FAPbI_3$ NCs have also shown potential as near-infrared emitters.[26]

Like halide perovskite thin films, the problem of inaccessibility of some stable alloy compositions still remains even in the case of NCs. Attempts have been made to directly alloy on the A site during synthesis.[26,66] For example, it was recently reported that the 700−800 nm emission range (from pure $CsPbI_3$ to pure $FAPbI_3$) in monohalide $Cs_{1-x}FA_xPbI_3$ NCs cannot be achieved just by varying the A-site cation precursor amount via direct NC synthesis due to differences in precursor reactivity. It was then stated that the only way to achieve the tunability (emission between 710 and 750 nm) is to exploit the quantum confinement effect, which is not the most-suitable way in terms of the stability of the final alloyed products.[66]

Herein, we report the synthesis of $Cs_{1-x}FA_xPbI_3$ colloidal alloyed NCs by post-synthetic cation exchange. Cation exchange, as opposed to anion exchange, in perovskite materials is more rare.[42−46,67] However, by combining colloidal solutions of $CsPbI_3$ and $FAPbI_3$ NCs in appropriate proportions along with modest heating allows the cross-exchange between the A-site cations to result in desired alloy compositions retaining their crystallographic framework (as schematically depicted in Figure 1A). We can thus fine-tune across the whole composition range, obtaining stable perov-

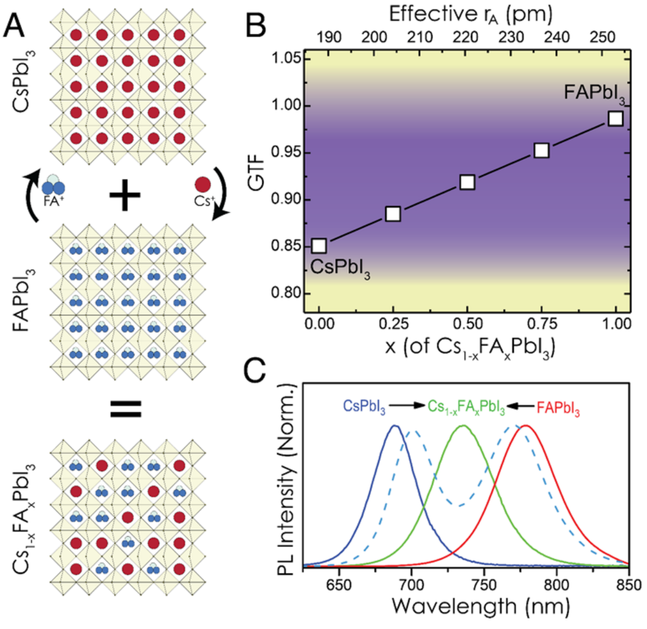

Figure 1. A-site ion exchange to form phase stable $Cs_{1-x}FA_xPbI_3$ NCs. (A) Schematic diagram showing the cross-exchange of Cs^+ and FA^+ ions between $CsPbI_3$ and $FAPbI_3$ perovskite NCs. (B) Goldschmidt tolerance factor as a function of FA^+ ion concentration shows that all compositions are expected to be phase-stable (the purple region in the plot). Top axis shows the effective or average A-site radius. (C) PL emission spectra depicting how $CsPbI_3$ and $FAPbI_3$ NCs convert into alloyed NCs; the dashed curve indicates the emission profile of one of the early stages of alloying.

DOI: 10.1021/acsnano.8b05555
ACS Nano XXXX, XXX, XXX−XXX

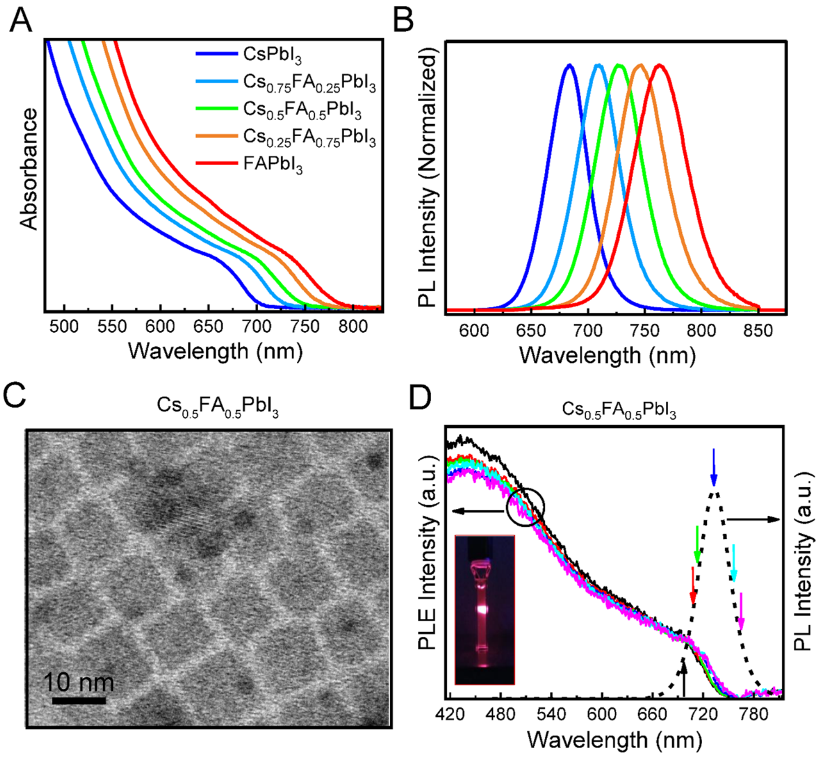

Figure 2. Optical and TEM characterization of the $Cs_{1-x}FA_xPbI_3$ NCs. (A) UV−vis absorption and (B) PL emission spectra of the alloyed NCs showing tunability over ∼650−800 nm range. (C) TEM image of $Cs_{0.5}FA_{0.5}PbI_3$ NCs. (D) Photoluminescence excitation spectra of $Cs_{0.5}FA_{0.5}PbI_3$ NCs (the corresponding PL emission spectrum is shown with a dashed line) at different emission energies shows the absence of substantial inhomogeneous broadening of the PL emission due to alloying; the PLE spectra were collected at emission wavelengths indicated by the color-coded vertical arrows. The inset in panel D shows a photograph of the luminescence from $Cs_{0.5}FA_{0.5}PbI_3$ NCs under UV illumination.

skite phases (see Figure 1B), which otherwise have not been achieved via direct synthesis, or in large-grain thin-film perovskite for the reasons stated above. Controllable and tunable emission in ∼650−800 nm range in lead iodide perovskite NCs can thus be realized with the A-site cation composition as the only variable. We utilized the individual $CsPbI_3$ and $FAPbI_3$ NCs as "precursors" to yield a homogeneous alloy NC solution via continuous A-site cation exchange between them (Figure 1C). Photoluminescence (PL) kinetics at various alloying temperatures reveal that the interchange process is slower than the X-site ion exchange, and the activation energy related to this process is ∼0.65 eV. We applied the alloyed $Cs_{1-x}FA_xPbI_3$ QDs in solar cell devices that show more-optimal V_{OC} deficits compared with large-grain film-based devices of similar composition and E_G. The $Cs_{1-x}FA_xPbI_3$ QD devices also show low hysteresis and a power-conversion efficiency of ∼10%.

RESULTS AND DISCUSSION

To obtain the alloy compositions of $Cs_{1-x}FA_xPbI_3$, colloidal NCs of $CsPbI_3$ and $FAPbI_3$ are first synthesized using the hot-injection method. The individual colloidal solutions are then mixed in controlled ratios. Figure 2 shows the optical data of the resulting alloy NCs. As can be seen from Figure 2A,B, the absorption onset and the PL emission peak positions can be continuously tuned from pure $CsPbI_3$ to pure $FAPbI_3$ within the range of ∼650−800 nm. The time-resolved photoluminescence measurements reveal multiexponential PL decay behavior with average lifetimes in the range of 23−55 ns, with the $FAPbI_3$ exhibiting the slowest decay (see Figure S1). The as-prepared NCs show a quantum yield (QY) of ∼60−70%; after repeated cleaning with methyl acetate for the purpose of applying in the solar cells, and the NC solutions show QY of ∼40%. The transmission electron microscope (TEM) images (Figure 2C) show that the alloy NCs retain their original size and shape (also see Figure S2 for additional TEM images). Furthermore, when we alloy NCs of different sizes (*i.e.*, small $CsPbI_3$ NCs with PL maximum at ∼660 nm and larger $FAPbI_3$ NCs with PL maximum at ∼770 nm), we observe an asymmetric absorption with a bimodal distribution of particles and an asymmetric PL emission spectrum that can be deconvoluted with two Gaussians with peak maximum at ∼680 and ∼728 nm (see Figure S3A−C). This indicates that the NCs retain their original size, with the final composition being tuned by the relative amounts of Cs^+ to FA^+ total ions.

Photoluminescence emission (PLE) spectroscopy is often used to study inhomogeneous broadening of PL emission in NCs[68−71] and was employed here to examine the alloying in the $Cs_{1-x}FA_xPbI_3$ NCs. Figure 2D shows the PL of the $Cs_{0.5}FA_{0.5}PbI_3$ NCs and corresponding PLE spectra collected at different emission energies, as dictated by the color-coded arrow on the emission spectrum. The overlap of all of the PLE spectra indicate that they are independent of emission energies, and there is no significant inhomogeneous broadening of the PL emission due to alloying. PLE measurements on the other compositions also point to the absence of significant inhomogeneity in alloying (see Figure S4). However, the PLE spectra collected at different emission energies in case of the alloys resulted from intentionally mixing smaller $CsPbI_3$ and larger $FAPbI_3$ NCs clearly shows two distinct transitions at

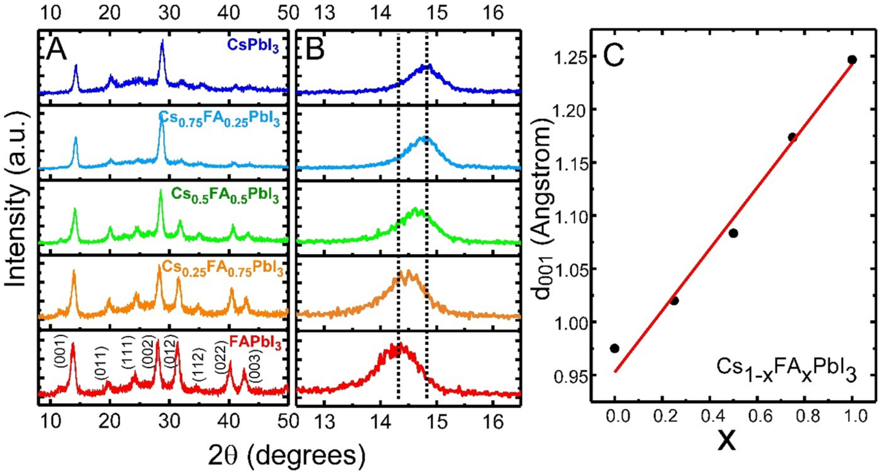

Figure 3. XRD of the $Cs_{1-x}FA_xPbI_3$ NCs. (A) Wide-angle XRD patterns of the alloyed NCs show the NCs retain their black, corner-sharing perovskite phase after alloying. The diffraction peaks for the $FAPbI_3$ NCs were indexed following Protesescu et al.[26] (B) Zoomed-in view of the (001) diffraction peak showing continuous shift from pure $FAPbI_3$ to pure $CsPbI_3$. (C) Vegard's law demonstrated by showing the linear shift of the d_{001} peak with composition.

~670 and ~700 nm (see Figure S3D), a result of either two alloy compositions or, more likely, homogeneous alloy composition with bimodal size distribution. The alloyed NCs retain their absorption and PL emission shape as well as their perovskite phase for months after the ion exchange procedure, indicating that the alloyed NCs reach equilibrium (see Figure S5).

Figure 3A shows the powder XRD patterns of the alloy NCs. As can be seen from the XRD patterns, all the alloy compositions retain their perovskite structure with prominent (001) and (002) peaks. The diffraction peaks shift monotonically between the patterns obtained with pure $CsPbI_3$ and $FAPbI_3$ NCs [see Figure 3B for a zoomed-in view of the XRD pattern showing the shift of the (001) peak]. It is to be noted here that previous studies have shown $CsPbI_3$ in bulk can have more than one perovskite phase with corner-shared octahedra. For example, neutron powder diffraction studies reveal that room temperature nonperovskite δ_o phase of $CsPbI_3$ (orthorhombic, *Pnma*) can be converted into cubic α phase (with undistorted corner shared $[PbI_6]^{4-}$ octahedra, *Pm*-3m) upon heating above 360 °C.[72,73] There can be two more perovskite phases of $CsPbI_3$ at temperatures lower than 360 °C depending upon the amount of tilting of the $[PbI_6]^{4-}$ octahedra: the β phase (260 °C) and the γ phase (175 °C).[73] These kinetically stabilized perovskite phases convert into the nonperovskite δ phase at room temperature in ambient conditions. However, $FAPbI_3$ has been shown to exist in the trigonal phase (space group *P*3*m*1) at room temperature,[14,73] although the ideal cubic perovskite phase with space group *Pm*-3m has also been reported in multiple studies.[17,74−76] We generated the powder X-ray diffraction patterns using the reported crystallographic information to compare with our $CsPbI_3$ and $FAPbI_3$ NCs (see Figure S6). We note here that both of them are stabilized in the perovskite phase at room temperature under ambient conditions,[26,56] although it is difficult to identify the exact amount of octahedral tilting and associated space group due to Scherrer broadening of the XRD peaks.

To obtain a particular composition of $Cs_{1-x}FA_xPbI_3$, it is necessary to know the starting concentration of $CsPbI_3$ and $FAPbI_3$ NCs in the colloidal solution. However, this is not straightforward without knowledge of the size-dependent molar extinction coefficient. While the size-dependent molar extinction coefficient for $CsPbBr_3$ NCs was recently published,[77] similar studies on $CsPbI_3$ and $FAPbI_3$ have not yet been reported. However, the energy levels of valence band maxima and conduction band minima in lead halide perovskites are formed from lead and halide *s* and *p* atomic orbitals,[78−80] and the density of states (DOS) near the band edges are similar for different $APbX_3$ perovskites if X is the same.[81] It is therefore reasonable to assume that colloidal solutions of similarly sized $CsPbI_3$ and $FAPbI_3$ NCs with similar optical density near the band gap will have similar concentration of NCs in the component solutions. With this assumption, we mix the individual $CsPbI_3$ and $FAPbI_3$ NC solutions with similar absorbance near the band edge (see Figure S7 for the raw absorption data) in different ratios. The XRD patterns and the PL emission spectra of all the compositions vary linearly with the presumed compositions (see Figures 3C and S8) validating our approximation of concentration.

To closely monitor the A-site cation cross-exchange between $CsPbI_3$ and $FAPbI_3$ NCs, we performed the mixing at various temperatures in the range of 45 to 90 °C. Unlike the X-site exchange, which occurs rapidly (time scale of 2 min),[42] the A-site exchange does not spontaneously occur at room temperature. The time-dependent PL measurements show that the two initial emission peaks merge into a single peak over time (the higher energy peak, referred to as E_1, corresponds to the Cs-rich composition, and the lower energy peak, referred to as E_2 ,corresponds to the FA-rich composition). As can be seen from Figure 4A−C (also shown in Figure S9), these two peaks do not move substantially from the original positions of $CsPbI_3$ and $FAPbI_3$ at room temperature at least up to ~40 min. The exchange is temperature-dependent; the high-energy and the low-energy peaks merge more rapidly at elevated solution temperature. For example, if we look at the PL emission spectral profile after 60 min at three different temperatures, the emission spectrum has two distinct peaks at 45 °C that have merged into a single peak at 90 °C. The emission energies of E_1 and E_2 over time are plotted in Figure S10A. If we assume

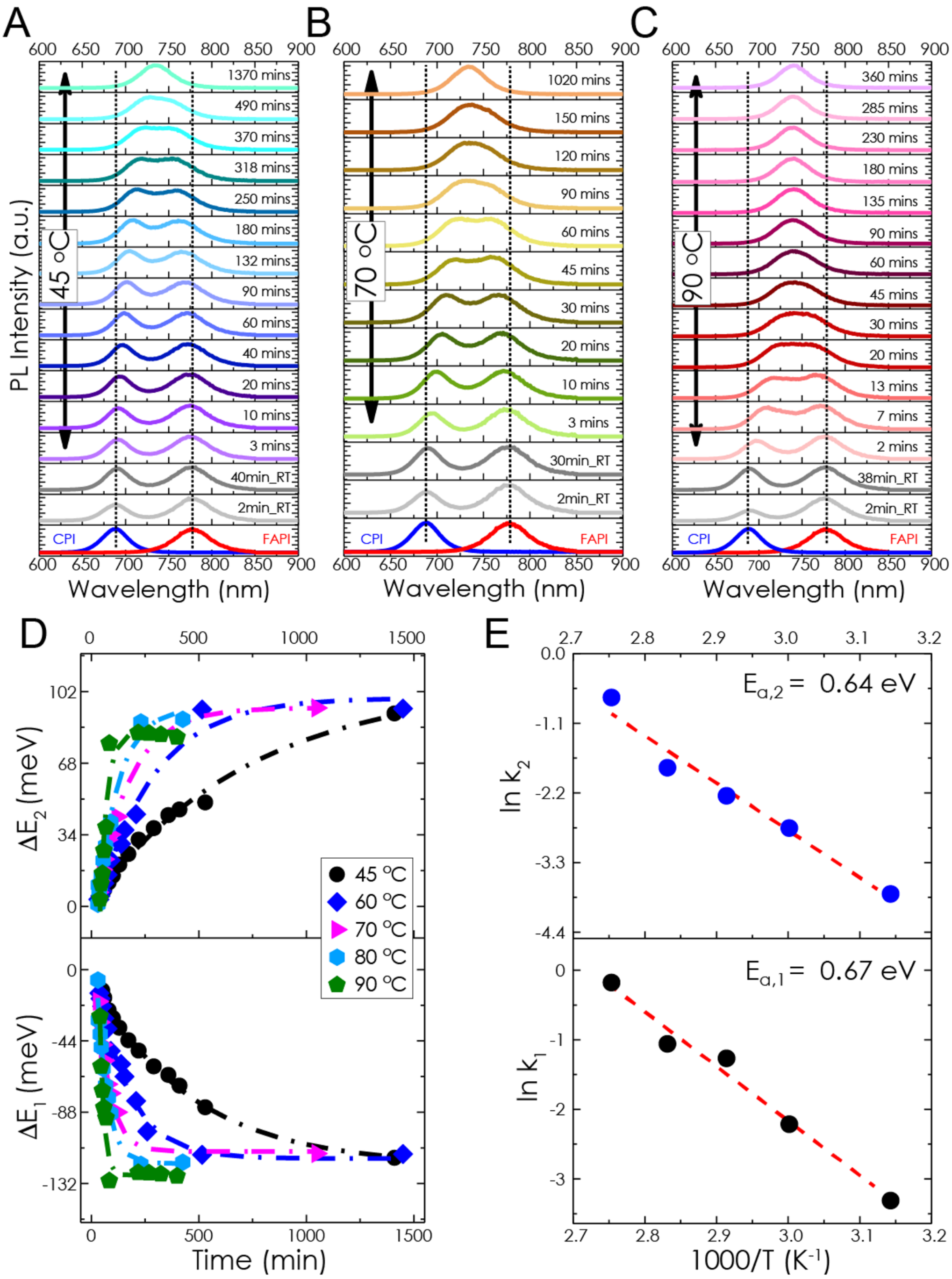

Figure 4. Temperature-dependent kinetics of A-site alloying. The evolution of PL emission peaks with time at reaction temperatures of (A) 45 °C, (B) 70 °C, and (C) 90 °C; the bottom-most spectra in these three figures show individual emission from $CsPbI_3$ (CPI, in blue) and $FAPbI_3$ (FAPI, in red). The next two spectra (shown in light and dark gray) are emissions at room temperature showing relatively stable peak positions. The remainder of the emission spectra are shown for the temporal evolution at elevated temperatures as labeled. (D) Shift in emission energy from their original position, depicting how the high-energy peak (E_1) is red-shifting from pure $CsPbI_3$ due to the incorporation of FA^+ and how the low-energy peak (E_2) is blue-shifting from pure $FAPbI_3$ due to incorporation of Cs^+ over time. The dotted lines are exponential fits to the experimental data. (E) Arrhenius plot showing the rates of conversion of $CsPbI_3$ (k_1, bottom panel) and $FAPbI_3$ (k_2, top panel) into $Cs_{1-x}FA_xPbI_3$ against $1/T$ (T being the absolute temperature). The dotted lines are linear fits to extract the activation energies ($E_{a,1}$ and $E_{a,2}$, respectively) for these processes.

that the change in PL peak position is linear with respect to composition, then the rate at which these peaks shift from emission energies of pure $CsPbI_3$ and $FAPbI_3$ can be related to how fast Cs^+ and FA^+ ions leave the starting NC and diffuse into the other NC. It remains experimentally difficult to decouple and monitor these two processes separately. Nonetheless, we observe that the rate of shift of the high-energy (ΔE_1) and the low-energy peaks (ΔE_2) can be reasonably fitted with single exponentials, indicating a first-order process, as shown in Figure 4D (also see Figure S10B in the SI for zoomed-in version). These rates can be used to extract the activation energy (E_a) related to the alloying process. Fitting these rates with the Arrhenius eq (Figure 4E) yields an activation energy of ~0.65 eV (see the Supporting Information for methods). This activation energy is higher than that reported for I^- diffusion in methylammonium and formamidinium lead iodide perovskites or Br^- and Cl^- interdiffusion in $CsPbCl_xBr_{1-x}$ nanowires (~0.45 eV).[82,83] However, it has been reported in theoretical studies that vacancy mediated diffusion of FA^+ ions has a surprisingly similar activation barrier of ~0.6 eV in bulk $FAPbI_3$.[82] The A-site alloying reported in this study is likely to be more complicated, involving multiple mechanisms potentially involving the NC surface ligands.

$Cs_{1-x}FA_xPbI_3$ NCs were used to fabricate photovoltaic devices with the device architecture shown in Figure 5. There are several potential advantages to using perovskite QDs in photovoltaic devices over large-grain perovskites. One main advantage is the phase stabilization of metastable $CsPbI_3$.[56,84,85] Second, ink for thin films is in the form of molecular precursors, and the homogeneity of the multicrystalline absorber layer on the device depends on the substrate and other parameters like solvent evaporation and temperature, during crystallization.[86] Using colloidal crystalline NC inks removes the substrate effects from the crystallization process (because it occurs previously in solution during synthesis), thus eliminating the need to precisely control the film morphology, crystallinity, and homogeneity. As reported previously, we used formamidinium iodide (FAI) as a surface treatment to replace the long-chain oleylammonium ligands.[64,85] The devices show stabilized power output (SPO) efficiencies of 8.8−10.9% with low hysteresis and up to ~75% external quantum efficiency (EQE) (see Figure 5C,D and Table 1 for a summary).

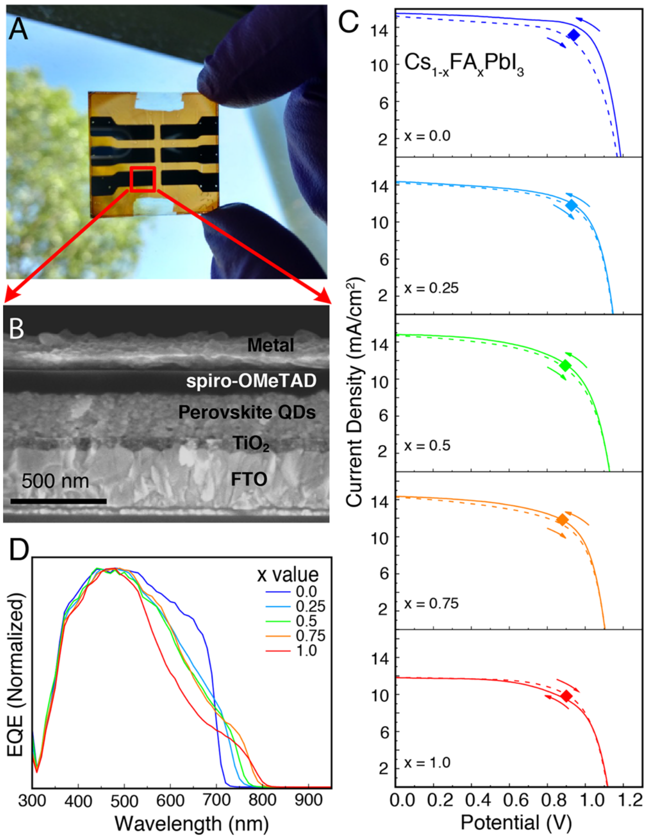

Figure 5. Solar-cell device performance of $FAPbI_3$ and the alloyed NCs. (A) Photograph of one of the solar cell devices. (B) The corresponding cross-sectional scanning electron microscopy image. (C) *J*−*V* curves for $Cs_{1-x}FA_xPbI_3$ QD devices; bottom to top: pure $FAPbI_3$, $Cs_{0.25}FA_{0.75}PbI_3$, $Cs_{0.50}FA_{0.50}PbI_3$, $Cs_{0.75}FA_{0.25}PbI_3$, pure $CsPbI_3$; the solid and dotted lines represent reverse and forward scans, respectively; the solid squares on the *J*−*V* curves shows the SPO values. (D) Normalized EQE scans for each composition showing the tunable onset position depending on the QD composition.

To directly compare the V_{OC} of QD solar cells to the more-traditional large-grain perovskite devices, we fabricated both types of solar cells. The V_{OC} for both perovskite NCs devices and large grain devices are compared as a function of the E_G and of the A-site composition (fraction of FA) and are shown in Figure 6 (also in Figure S12). The E_G values were extracted from the onset of the EQE spectra. For the large-grain devices, the A-site composition was tuned with a Cs fraction of 0 to 0.3 because of the previously mentioned challenge in crystallization of compositions with higher amounts of Cs. We obtained V_{OC} up to ~1.17 V in the QD devices, as compared to the previously mentioned 1.0 V in bulk $Cs_{1-x}FA_xPbI_3$ devices. All of our thin-film perovskite devices exhibit near state-of-the art V_{OC} (see also Table S1) compared to the literature for similar compositions and device architectures.

The quantum confinement effect in the NCs slightly increases the E_G of a particular composition, so it is more reasonable to compare the observed V_{OC} to that of the thermodynamic limit for the determined E_G (the dashed line in Figure 6A). We have plotted V_{OC}/V_{OC}^{MAX} against E_G in Figure 6B and against fraction of FA in Figure S12B. Here, V_{OC} is the observed open-circuit voltage, while V_{OC}^{MAX} is the maximum available open-circuit voltage for a single junction solar cell with the given bandgap energy as determined by the Shockley−Queisser (SQ) theoretical analysis.[87] This gives a comparative estimate of voltage loss in the devices. As seen in Figure 6, the V_{OC} loss is lower than that of the bulk perovskite devices at any particular composition or bandgap value. Another important finding to note here is that although the pure $FAPbI_3$ QD devices have somewhat lower efficiency, they exhibit the lowest V_{OC} loss, retaining approximately 89% of the voltage thermodynamically available for the given E_G.

CONCLUSIONS

In conclusion, we have demonstrated a methodology with which to synthesize colloidal $Cs_{1-x}FA_xPbI_3$ alloyed NCs via a post-synthetic A-site cation cross-exchange between $CsPbI_3$ and $FAPbI_3$ NCs. This method allows us to synthesize NCs with compositions that cannot be attained by direct synthesis or in the bulk. The activation energy related to the alloying process has been estimated to be ~0.65 eV, which is higher than that associated with halide exchange. The solar-cell performance with these alloyed NC inks shows increased voltage approaching the SQ limit compared with the bulk perovskite devices. We demonstrate the opportunity to expand the library of tunable perovskite NCs via cation exchanges. We postulate that a similar approach may also be applied to perform B-site cation exchange in the future that may lead to stable and tunable infrared-absorbing perovskite NCs.

METHODS

Materials. Cesium carbonate (Cs_2CO_3; 99.9%), oleic acid (OA; technical grade, 90%), oleylamine (OlAm; technical grade, 70%), 1-

DOI: 10.1021/acsnano.8b05555
ACS Nano XXXX, XXX, XXX−XXX

Table 1. Solar-Cell Device Parameters of the $Cs_{1-x}FA_xPbI_3$ QD Devices

	reverse				forward				
	V_{OC} (V)	J_{SC} (mA/cm^2)	FF	PCE (%)	V_{OC} (V)	J_{SC} (mA/cm^2)	FF	PCE (%)	SPO(%)
$FAPbI_3$	1.12	11.81	0.64	8.52	1.12	11.85	0.68	9.01	8.83
$Cs_{0.25}FA_{0.75}PbI_3$	1.1	14.37	0.66	10.41	1.11	14.35	0.63	10.05	10.41
$Cs_{0.5}FA_{0.5}PbI_3$	1.13	14.8	0.62	10.42	1.13	14.7	0.6	10.05	10.26
$Cs_{0.75}FA_{0.25}PbI_3$	1.15	14.36	0.68	11.14	1.14	14.23	0.66	10.77	10.93
$CsPbI_3$	1.18	15.5	0.73	13.47	1.17	15.2	0.66	11.75	12.37

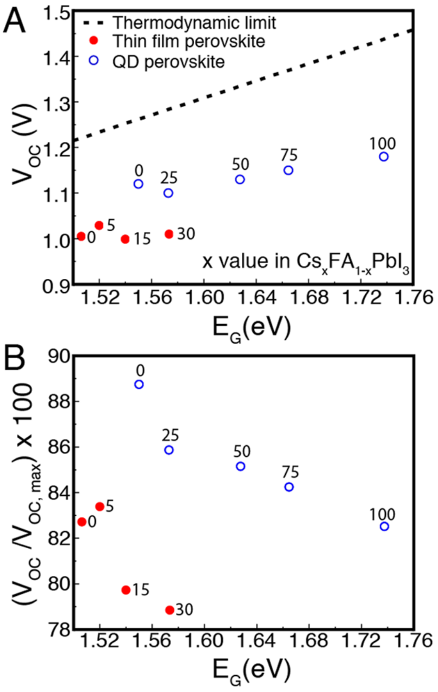

Figure 6. Estimation of voltage loss in the perovskite NC and thin-film devices. (A) Experimental V_{OC}s and (B) fraction of observed V_{OC} compared to the maximum attainable V_{OC} as functions of E_G; the dashed line in panel A represents the theoretical thermodynamic limit for open-circuit voltage in single-junction solar cells as a function of the bandgap value and was generated using the data in ref 90. The numbers beside the solid and open circles represent the x in the $Cs_xFA_{1-x}PbI_3$ alloys.

octadecene (1-ODE; technical grade, 90%), hexane (reagent grade, ≥ 95%), octane (anhydrous, ≥ 99%), methyl acetate (MeOAc, anhydrous, 99.5%), lead nitrate ($Pb(NO_3)_2$, 99.999%), ethyl acetate (EtOAc, anhydrous, 99.8%), cesium iodide (CsI, 99.999%), formamidinium acetate (FA-acetate, 99%), titanium ethoxide (≥97%), hydrochloric acid (HCl; 37% in water), titanium diisopropoxide bis(acetylacetonate) (TAA, 75 wt % in iso-propanol), chlorobenzene (anhydrous, 99.8%), acetonitrile (anhydrous, 99.8%), toluene (anhydrous, 99.8%), 4-*tert*-butylpyridine (4-TBP; 96%), dimethylformamide (DMF), and dimethyl sulfoxide (DMSO) were purchased from Sigma-Aldrich. 2,2′,7,7′-Tetrakis(*N*,*N*-di-p methoxyphenylamine)-9,9′-spirobifluorene (spiro-OMeTAD; ≥ 99.5%) was purchased from Lumtec. Bis(trifluoromethane)sulfonimide lithium salt (Li-TFSI) and PbI_2 (99.9985%) were purchased from Alfa Aesar. Formamidium iodide (FAI) was purchased from Dyesol.

Synthesis of $CsPbI_3$ NCs. $CsPbI_3$ NCs were synthesized following previously reported method[56] with slight modifications. Briefly, 1.08 mmol (0.5 g) PbI_2 and 25 mL of 1-ODE were degassed under vacuum at 120 °C for 30 min inside a three-necked round-bottom flask. A mixture of 2.5 mL of OA and 2.5 mL of OlAm, preheated to 120 °C, was injected into the reaction flask under vacuum. The mixture was briefly degassed until the PbI_2 dissolved to form a clear solution. Then the reaction mixture was heated to 180 °C under N_2 flow. At 180 °C, 2 mL of the Cs-oleate solution was swiftly injected into the PbI_2 mixture, and the reaction mixture was immediately quenched in an ice-water bath. To separate the $CsPbI_3$ NCs from the reaction liquor, 70 mL of MeOAc was added to the colloidal solution at room temperature and centrifuged at 7500 rpm for 5 min. The resulting precipitate was dispersed in 5 mL of hexane, re-precipitated with 5 mL MeOAc, and centrifuged again at 7500 rpm for 5 min. The resulting NCs were dispersed in 15 mL of hexane and stored in the refrigerator until used. To prepare solutions for spin coating and cation exchange, the $CsPbI_3$ NCs in hexane were removed from the refrigerator and centrifuged at 7500 for 5 min. The precipitate was discarded. The hexane from the supernatant was evaporated, and the NCs were finally redispersed in 1−2 mL of octane.

Synthesis of $FAPbI_3$ NCs. The $FAPbI_3$ NCs were synthesized following a method reported by Protesescu et al.[26] with slight modifications. Briefly, 0.74 mmol (0.344 g) PbI_2 and 20 mL 1-ODE were degassed under a vacuum at 120 °C for 30 min. A mixture of 4 mL of OA and 2 mL of OlAm, preheated to 120 °C, was then injected into the PbI_2 mixture under a vacuum. The mixture was briefly degassed under a vacuum until the PbI_2 mixture became clear. Under N_2 flow, the temperature was reduced to 80 °C. At 80 °C, 5 mL of the FA−oleate solution was swiftly injected into the PbI_2 mixture. After 5 s of reaction time, the reaction mixture was quenched using an ice-water bath. After the mixture cooled to room temperature, 1 mL of toluene and 5 mL of MeOAc were added, and the mixture was centrifuged at 8000 rpm for 30 min. The resulting NC precipitate was dispersed in 7 mL of toluene, re-precipitated with 5 mL of MeOAc, and centrifuged at 8000 rpm for 10 min. The final precipitate was redispersed in 5−7 mL of octane and stored under nitrogen for further use. The concentration of the $FAPbI_3$ NCs was adjusted to be comparable to that of the $CsPbI_3$ NC solution before synthesis of the alloys or fabrication of devices.

Synthesis of $Cs_{1-x}FA_xPbI_3$ Alloys. Colloidal solutions of $CsPbI_3$ and $FAPbI_3$ NCs dispersed in octane were mixed in different ratios to produce the desired Cs/FA stoichiometry. Before mixing, the absorption spectra of the individual samples were measured, and the concentration was adjusted so that each solution had a similar optical density near the band edge. The mixture was either left to react for 48 h at room temperature or reacted at different temperature (a maximum of 90 °C) for kinetics study.

Perovskite QD Device Fabrication. All of the solar devices were fabricated following earlier reported literature.[64] Briefly, a ∼50 nm TiO_2 layer was deposited on a patterned FTO-coated glass substrate (Thin Film Devices, Inc.; precleaned via sonication in iso-propanol and then UV−ozone treated for 10 min). The sol−gel TiO_2 was prepared by mixing 5 mL of ethanol, 2 drops of HCl, 125 μL of deionized water, and 375 μL of titanium ethoxide and stirred continuously for 48 h. The TiO_2 solution was filtered through a 0.20 μm polyvinylidene difluoride filter before use. The sol−gel TiO_2 was spin-cast on the FTO−glass substrate at 3000 rpm for 30 s, annealed at 450 °C for 30 min. A total of four layers (∼300 nm thick) of the QD absorber ink was then deposited layer-by-layer at 1000 rpm for 20 s followed by 2000 rpm for 5 s. The ligand-exchange steps during the QD layer deposition involved dipping (for ∼1−2 s) the device in a saturated solution of $Pb(NO_3)_2$ in MeOAc (prepared by sonicating 20 mg $Pb(NO_3)_2$ in 20 mL of MeOAc for ∼10 min and then removing the excess salt by centrifuging at 3500 for 5 min) after each layer deposition followed by rinsing with neat MeOAc and drying immediately with a jet of dry air. After these steps were repeated for 4 or 5 QD layers, the devices were finally soaked in a saturated solution of FAI in EtOAc (prepared by sonicating ~20 mg of FAI salt in ~30 mL of EtOAc for ~15 min and then removing the excess salt by centrifuging at 3500 for 5 min) for ~10 s, followed by rinsing with neat MeOAc. The hole transporting materials was prepared by mixing 72.3 mg of spiro-OMeTAD, 28.8 mL of 4-TBP, 1 mL of chlorobenzene, and 17.5 mL of Li-TFSI stock solution (520 mg/mL in acetonitrile). The spiro-OMeTAD solution was then spin-cast on the QD absorber layer at 5000 rpm for 30 s. All deposition and ligand-treatment procedures were performed in an ambient condition at relative humidity of ~25–30%. The devices were left in the drybox overnight before depositing the top electrodes. MoO_x was deposited at a rate of 0.1–0.5 Å/s at a base pressure lower than 2×10^{-7} Torr for a total thickness of 15 nm. Aluminum electrodes were evaporated at a rate ranging from 0.5 to 2 Å/s for a total thickness of 120 nm.

Perovskite Thin-Film Device Fabrication. $FAPbI_3$ thin-film devices were fabricated following previously reported study.[29] Briefly, a thin compact TiO_2 layer with ~30 nm thickness was first spin-cast (700 rpm for 10 s, 1000 rpm for 10 s, and 2000 rpm for 30 s) on cleaned, patterned, FTO-coated glass substrates from a 0.2 M TAA solution in 1-butanol. The TiO_2/FTO/glass substrate was then annealed at 130 °C for 5 min and at 450 °C for 60 min. A 0.7 M stoichiometric FAI and PbI_2 solution in anhydrous DMF was prepared inside a glovebox and vortexed for 20 min at room temperature. The resulting clear, bright-yellow solution was filtered through a 0.20 μm polyvinylidene difluoride filter and spin-cast inside a glovebox on the compact TiO_2/FTO substrate by a consecutive three-step process: 500 rpm for 3 s, 3500 rpm for 10 s, and 5000 rpm for 30 s. A total of 1–2 s before the end of second step, a drop of toluene was gently placed on the spinning substrate. The resultant films were annealed at 170 °C for 1 min. For FA/Cs alloys, absorber layers were deposited following Zhen et al.[16] Briefly, inside a glovebox, stoichiometric amounts of FAI, CsI and PbI_2 were dissolved in a mixed solvent of DMSO and DMF (v/v = 3:7) to obtain precursor solutions of $Cs_{1-x}FA_xPbI_3$. All of the solutions were dissolved at room temperature by vortexing, and they are filtered through 0.20 μm polyvinylidene difluoride filters before use. The solutions were then spin-cast on the TiO_2/FTO/glass substrate using the following recipe: (1) 100 rpm for 3 s, (2) 3500 rpm for 10 s, (3) 5000 rpm for 30 s. During step 3, after 20 s, 1 mL of toluene was deposited on the spinning substrate. The films were annealed at 170 °C for 10 min. Further layers, including spiro-OMeTAD deposition and the electrode depositions, were similar to that of the QD devices mentioned above except gold electrodes were deposited instead of aluminum electrodes. All of the depositions were done inside a nitrogen-filled glovebox.

Device Characterizations. All of the devices were tested using a Newport Oriel Sol3A solar simulator with a xenon lamp source inside a N_2-filled glovebox. A KG5 filtered Si reference diode was used to calibrate the lamp intensity to 100 mW/cm^2 (AM1.5) and minimize the spectral mismatch of the lamp source. Devices were illuminated through a metal aperture (0.058 cm^2). The devices were tested in forward scan and reverse san at a scan rate of 20 mV/s. Stabilized power output was measured by holding the device at a constant voltage corresponding to the voltage at the maximum power point of a previous $J-V$ scan. EQE measurements were taken using a Newport Oriel IQE200 system.

Calculation of Goldschmidt Tolerance Factor. The GTFs for all of the alloy compositions of $Cs_{1-x}FA_xPbI_3$ were calculated using the following formula:

$$t = \frac{[x \cdot r_{Cs} + (1 - x) \cdot r_{FA}] + r_X}{\sqrt{2}\,(r_{Pb} + r_X)}$$

where r_i is the ionic radius of the individual species. The Shannon ionic radius for Cs^+, Pb^{2+}, and I^- were used,[88] while the reported effective radius for FA^+ was used for the following calculations:[22,89] r_{Cs} = 188 pm, r_{Pb} = 119 pm, r_I = 220 pm, and r_{FA} = 253 pm.

Estimation of Activation Energy. To calculate the activation energy for the A-site cation exchange, $CsPbI_3$ and $FAPbI_3$ nanocrystal solutions (1:1 ratio) were mixed at 45, 60, 70, 80, and 90 °C, and aliquots were taken at different time intervals for PL emission measurements. The PL emission spectra were then fitted with Gaussian functions to extract the peak emission energies. Before reaching a thermodynamically stable state with a single emission peak, the PL emission spectra of the intermediate aliquots could be resolved and fitted well with two Gaussians. The high-energy peak (denoted E_1) is indicative of high-Cs-containing alloys, and the low-energy peak (E_2) is indicative of high-FA-containing alloys in an ensemble of nanocrystals. The shift of E_1 (ΔE_1) and E_2 (ΔE_2) from pure $CsPbI_3$ and pure $FAPbI_3$ emission positions, respectively, were found to be exponential as a function of time for all temperatures. The rate at which the emission energies (k) shift was extracted from exponential fitting. The activation energy, E_a, was then calculated using the Arrhenius equation:

$$k = A_o \exp\left[-\frac{E_a}{k_B T}\right]$$

Or,

$$\ln(k) = \left(-\frac{E_a}{k_B}\right)\frac{1}{T} + \ln(A_o)$$

where k_B is the Boltzmann constant, T is the absolute temperature, and A_0 is the pre-exponential factor.

ASSOCIATED CONTENT

Supporting Information

The Supporting Information is available free of charge on the ACS Publications website at DOI: 10.1021/acsnano.8b05555.

Additional details, figures, and tables related to the preparation of precursors and characterization details (PDF)

AUTHOR INFORMATION

Corresponding Author

*E-mail: joey.luther@nrel.gov.

ORCID

Abhijit Hazarika: 0000-0003-0391-2163
Jeffrey A. Christians: 0000-0002-6792-9741
Joseph J. Berry: 0000-0003-3874-3582
Justin C. Johnson: 0000-0002-8874-6637
Joseph M. Luther: 0000-0002-4054-8244

Notes

The authors declare no competing financial interest.

ACKNOWLEDGMENTS

This work was authored by Alliance for Sustainable Energy, LLC, the manager and operator of the National Renewable Energy Laboratory for the U.S. Department of Energy (DOE) under contract no. DE-AC36-08GO28308. We acknowledge the Department of Defense Operational Energy Capability Improvement Fund (OECIF) for development of the QD solar cells with mixed cation. The device architecture and optical characterization was supported by the Center for Advanced Solar Photophysics and the Energy Frontier Research Center funded by the U.S. Department of Energy, Office of Science, Office of Basic Energy Sciences. Control samples of thin film perovskites and structural characterization was performed by authors supported by the hybrid perovskite solar cell program funded by the U.S. Department of Energy Office of Energy

Efficiency and Renewable Energy Solar Energy Technologies Office. Cation exchange on perovskite was developed under the NREL Laboratory Directed Research and Development program. Q.Z. acknowledges fellowship support from the China Scholarship Council. J.A.C. was supported by the DOE Office of Energy Efficiency and Renewable Energy Postdoctoral Research Award through the Solar Energy Technologies Office under DOE contract no. DE-SC00014664. E.A.G. acknowledges support from the Director's Fellowship program of the National Renewable Energy Laboratory. We thank Ross Larsen for helpful discussion on determination of the activation energy and Rens Limpens for assistance on determining the PLQY. The views expressed in the article do not necessarily represent the views of the DOE or the U.S. Government.

REFERENCES

(1) NREL. Best Research-Cell Efficiencies. https://www.nrel.gov/pv/assets/pdfs/pv-efficiencies-07-17-2018.pdf (accessed August 28, 2018).

(2) Manser, J. S.; Christians, J. A.; Kamat, P. V. Intriguing Optoelectronic Properties of Metal Halide Perovskites. *Chem. Rev.* **2016**, *116*, 12956−13008.

(3) Yang, W. S.; Park, B.-W.; Jung, E. H.; Jeon, N. J.; Kim, Y. C.; Lee, D. U.; Shin, S. S.; Seo, J.; Kim, E. K.; Noh, J. H.; Seok, S. I. Iodide Management in Formamidinium-Lead-Halide−Based Perovskite Layers for Efficient Solar Cells. *Science* **2017**, *356*, 1376−1379.

(4) Lin, Q.; Armin, A.; Burn, P. L.; Meredith, P. Organohalide Perovskites for Solar Energy Conversion. *Acc. Chem. Res.* **2016**, *49*, 545−553.

(5) Gao, P.; Gratzel, M.; Nazeeruddin, M. K. Organohalide Lead Perovskites for Photovoltaic Applications. *Energy Environ. Sci.* **2014**, *7*, 2448−2463.

(6) Stranks, S. D.; Snaith, H. J. Metal-Halide Perovskites for Photovoltaic and Light-Emitting Devices. *Nat. Nanotechnol.* **2015**, *10*, 391−402.

(7) Docampo, P.; Bein, T. A Long-Term View on Perovskite Optoelectronics. *Acc. Chem. Res.* **2016**, *49*, 339−346.

(8) Tan, Z.-K.; Moghaddam, R. S.; Lai, M. L.; Docampo, P.; Higler, R.; Deschler, F.; Price, M.; Sadhanala, A.; Pazos, L. M.; Credgington, D.; Hanusch, F.; Bein, T.; Snaith, H. J.; Friend, R. H. Bright Light-Emitting Diodes Based on Organometal Halide Perovskite. *Nat. Nanotechnol.* **2014**, *9*, 687−692.

(9) Aygüler, M. F.; Weber, M. D.; Puscher, B. M. D.; Medina, D. D.; Docampo, P.; Costa, R. D. Light-Emitting Electrochemical Cells Based on Hybrid Lead Halide Perovskite Nanoparticles. *J. Phys. Chem. C* **2015**, *119*, 12047−12054.

(10) Yuan, M.; Quan, L. N.; Comin, R.; Walters, G.; Sabatini, R.; Voznyy, O.; Hoogland, S.; Zhao, Y.; Beauregard, E. M.; Kanjanaboos, P.; Lu, Z.; Kim, D. H.; Sargent, E. H. Perovskite Energy Funnels for Efficient Light-Emitting Diodes. *Nat. Nanotechnol.* **2016**, *11*, 872−877.

(11) Stoumpos, C. C.; Kanatzidis, M. G. Halide Perovskites: Poor Man's High-Performance Semiconductors. *Adv. Mater.* **2016**, *28*, 5778−5793.

(12) Kojima, A.; Teshima, K.; Shirai, Y.; Miyasaka, T. Organometal Halide Perovskites as Visible-Light Sensitizers for Photovoltaic Cells. *J. Am. Chem. Soc.* **2009**, *131*, 6050−6051.

(13) Lee, M. M.; Teuscher, J.; Miyasaka, T.; Murakami, T. N.; Snaith, H. J. Efficient Hybrid Solar Cells Based on Meso-Superstructured Organometal Halide Perovskites. *Science* **2012**, *338*, 643−647.

(14) Stoumpos, C. C.; Malliakas, C. D.; Kanatzidis, M. G. Semiconducting Tin and Lead Iodide Perovskites with Organic Cations: Phase Transitions, High Mobilities, and Near-Infrared Photoluminescent Properties. *Inorg. Chem.* **2013**, *52*, 9019−9038.

(15) Christians, J. A.; Schulz, P.; Tinkham, J. S.; Schloemer, T. H.; Harvey, S. P.; Tremolet de Villers, B. J.; Sellinger, A.; Berry, J. J.; Luther, J. M. Tailored Interfaces of Unencapsulated Perovskite Solar Cells For > 1,000 h Operational Stability. *Nat. Energy* **2018**, *3*, 68−74.

(16) Li, Z.; Yang, M.; Park, J.-S.; Wei, S.-H.; Berry, J. J.; Zhu, K. Stabilizing Perovskite Structures by Tuning Tolerance Factor: Formation of Formamidinium and Cesium Lead Iodide Solid-State Alloys. *Chem. Mater.* **2016**, *28*, 284−292.

(17) Liu, T.; Zong, Y.; Zhou, Y.; Yang, M.; Li, Z.; Game, O. S.; Zhu, K.; Zhu, R.; Gong, Q.; Padture, N. P. High-Performance Formamidinium-Based Perovskite Solar Cells *via* Microstructure-Mediated δ-to-α Phase Transformation. *Chem. Mater.* **2017**, *29*, 3246−3250.

(18) Lee, J. W.; Kim, D. H.; Kim, H. S.; Seo, S. W.; Cho, S. M.; Park, N. G. Formamidinium and Cesium Hybridization for Photo- and Moisture-Stable Perovskite Solar Cell. *Adv. Energy Mater.* **2015**, *5*, 1501310.

(19) Yi, C.; Luo, J.; Meloni, S.; Boziki, A.; Ashari-Astani, N.; Gratzel, C.; Zakeeruddin, S. M.; Rothlisberger, U.; Gratzel, M. Entropic Stabilization of Mixed A-Cation ABX$_3$ Metal Halide Perovskites for High Performance Perovskite Solar Cells. *Energy Environ. Sci.* **2016**, *9*, 656−662.

(20) Xia, X.; Wu, W.; Li, H.; Zheng, B.; Xue, Y.; Xu, J.; Zhang, D.; Gao, C.; Liu, X. Spray Reaction Prepared FA$_{1\text{-}X}$Cs$_x$PbI$_3$ Solid Solution as A Light Harvester for Perovskite Solar Cells with Improved Humidity Stability. *RSC Adv.* **2016**, *6*, 14792−14798.

(21) Goldschmidt, V. M. Die Gesetze der Krystallochemie. *Naturwissenschaften* **1926**, *14*, 477−485.

(22) Kieslich, G.; Sun, S.; Cheetham, A. K. Solid-State Principles Applied to Organic-Inorganic Perovskites: New Tricks for An Old Dog. *Chem. Sci.* **2014**, *5*, 4712−4715.

(23) Green, M. A.; Ho-Baillie, A.; Snaith, H. J. The Emergence of Perovskite Solar Cells. *Nat. Photonics* **2014**, *8*, 506−514.

(24) Travis, W.; Glover, E. N. K.; Bronstein, H.; Scanlon, D. O.; Palgrave, R. G. On the Application of the Tolerance Factor to Inorganic and Hybrid Halide Perovskites: A Revised System. *Chem. Sci.* **2016**, *7*, 4548−4556.

(25) Saparov, B.; Mitzi, D. B. Organic−Inorganic Perovskites: Structural Versatility for Functional Materials Design. *Chem. Rev.* **2016**, *116*, 4558−4596.

(26) Protesescu, L.; Yakunin, S.; Kumar, S.; Bär, J.; Bertolotti, F.; Masciocchi, N.; Guagliardi, A.; Grotevent, M.; Shorubalko, I.; Bodnarchuk, M. I.; Shih, C.-J.; Kovalenko, M. V. Dismantling the "Red Wall" of Colloidal Perovskites: Highly Luminescent Formamidinium and Formamidinium−Cesium Lead Iodide Nanocrystals. *ACS Nano* **2017**, *11*, 3119−3134.

(27) Lin, Y.; Chen, B.; Zhao, F.; Zheng, X.; Deng, Y.; Shao, Y.; Fang, Y.; Bai, Y.; Wang, C.; Huang, J. Matching Charge Extraction Contact for Wide-Bandgap Perovskite Solar Cells. *Adv. Mater.* **2017**, *29*, 1700607.

(28) Khadka, D. B.; Shirai, Y.; Yanagida, M.; Noda, T.; Miyano, K. Tailoring the Open-Circuit Voltage Deficit of Wide-Band-Gap Perovskite Solar Cells Using Alkyl Chain-Substituted Fullerene Derivatives. *ACS Appl. Mater. Interfaces* **2018**, *10*, 22074−22082.

(29) Pool, V. L.; Dou, B.; Van Campen, D. G.; Klein-Stockert, T. R.; Barnes, F. S.; Shaheen, S. E.; Ahmad, M. I.; van Hest, M. F. A. M.; Toney, M. F. Thermal Engineering of FAPbI$_3$ Perovskite Material *via* Radiative Thermal Annealing and *in situ* XRD. *Nat. Commun.* **2017**, *8*, 14075.

(30) Eperon, G. E.; Paterno, G. M.; Sutton, R. J.; Zampetti, A.; Haghighirad, A. A.; Cacialli, F.; Snaith, H. J. Inorganic Caesium Lead Iodide Perovskite Solar Cells. *J. Mater. Chem. A* **2015**, *3*, 19688−19695.

(31) Kubicki, D. J.; Prochowicz, D.; Hofstetter, A.; Zakeeruddin, S. M.; Grätzel, M.; Emsley, L. Phase Segregation in Potassium-Doped Lead Halide Perovskites from 39K Solid-State NMR at 21.1 T. *J. Am. Chem. Soc.* **2018**, *140*, 7232−7238.

(32) Nazarenko, O.; Yakunin, S.; Morad, V.; Cherniukh, I.; Kovalenko, M. V. Single Crystals of Caesium Formamidinium Lead

Halide Perovskites: Solution Growth and Gamma Dosimetry. *NPG Asia Mater.* **2017**, *9*, e373.

(33) Son, D. H.; Hughes, S. M.; Yin, Y.; Alivisatos, A. P. Cation Exchange Reactions in Ionic Nanocrystals. *Science* **2005**, *36*, 1009−1012.

(34) Pietryga, J. M.; Werder, D. J.; Williams, D. J.; Casson, J. L.; Schaller, R. D.; Klimov, V. I.; Hollingsworth, J. A. Utilizing the Lability of Lead Selenide to Produce Heterostructured Nanocrystals with Bright, Stable Infrared Emission. *J. Am. Chem. Soc.* **2008**, *130*, 4879−4885.

(35) Luther, J. M.; Zheng, H.; Sadtler, B.; Alivisatos, A. P. Synthesis of PbS Nanorods and Other Ionic Nanocrystals of Complex Morphology by Sequential Cation Exchange Reactions. *J. Am. Chem. Soc.* **2009**, *131*, 16851−16857.

(36) Beberwyck, B. J.; Alivisatos, A. P. Ion Exchange Synthesis of III−V Nanocrystals. *J. Am. Chem. Soc.* **2012**, *134*, 19977−19980.

(37) Routzahn, A. L.; Jain, P. K. Single-Nanocrystal Reaction Trajectories Reveal Sharp Cooperative Transitions. *Nano Lett.* **2014**, *14*, 987−992.

(38) De Trizio, L.; Gaspari, R.; Bertoni, G.; Kriegel, I.; Moretti, L.; Scotognella, F.; Maserati, L.; Zhang, Y.; Messina, G. C.; Prato, M.; Marras, S.; Cavalli, A.; Manna, L. Cu$_{3-x}$P Nanocrystals as a Material Platform for Near-Infrared Plasmonics and Cation Exchange Reactions. *Chem. Mater.* **2015**, *27*, 1120−1128.

(39) Li, H.; Zanella, M.; Genovese, A.; Povia, M.; Falqui, A.; Giannini, C.; Manna, L. Sequential Cation Exchange in Nanocrystals: Preservation of Crystal Phase and Formation of Metastable Phases. *Nano Lett.* **2011**, *11*, 4964−4970.

(40) Akkerman, Q. A.; Genovese, A.; George, C.; Prato, M.; Moreels, I.; Casu, A.; Marras, S.; Curcio, A.; Scarpellini, A.; Pellegrino, T.; Manna, L.; Lesnyak, V. From Binary Cu$_2$S to Ternary Cu−In−S and Quaternary Cu−In−Zn−S Nanocrystals with Tunable Composition *via* Partial Cation Exchange. *ACS Nano* **2015**, *9*, 521−531.

(41) Rivest, J. B.; Jain, P. K. Cation Exchange on the Nanoscale: An Emerging Technique for New Material Synthesis, Device Fabrication, and Chemical Sensing. *Chem. Soc. Rev.* **2013**, *42*, 89−96.

(42) Nedelcu, G.; Protesescu, L.; Yakunin, S.; Bodnarchuk, M. I.; Grotevent, M. J.; Kovalenko, M. V. Fast Anion-Exchange in Highly Luminescent Nanocrystals of Cesium Lead Halide Perovskites (CsPbX$_3$, X = Cl, Br, I). *Nano Lett.* **2015**, *15*, 5635−5640.

(43) Akkerman, Q. A.; D'Innocenzo, V.; Accornero, S.; Scarpellini, A.; Petrozza, A.; Prato, M.; Manna, L. Tuning the Optical Properties of Cesium Lead Halide Perovskite Nanocrystals by Anion Exchange Reactions. *J. Am. Chem. Soc.* **2015**, *137*, 10276−10281.

(44) Ramasamy, P.; Lim, D.-H.; Kim, B.; Lee, S.-H.; Lee, M.-S.; Lee, J.-S. All-Inorganic Cesium Lead Halide Perovskite Nanocrystals for Photodetector Applications. *Chem. Commun.* **2016**, *52*, 2067−2070.

(45) Bekenstein, Y.; Koscher, B. A.; Eaton, S. W.; Yang, P.; Alivisatos, A. P. Highly Luminescent Colloidal Nanoplates of Perovskite Cesium Lead Halide and Their Oriented Assemblies. *J. Am. Chem. Soc.* **2015**, *137*, 16008−16011.

(46) Koscher, B. A.; Bronstein, N. D.; Olshansky, J. H.; Bekenstein, Y.; Alivisatos, A. P. Surface- vs Diffusion-Limited Mechanisms of Anion Exchange in CsPbBr$_3$ Nanocrystal Cubes Revealed through Kinetic Studies. *J. Am. Chem. Soc.* **2016**, *138*, 12065−12068.

(47) Bi, C.; Wang, S.; Wen, W.; Yuan, J.; Cao, G.; Tian, J. Room-Temperature Construction of Mixed-Halide Perovskite Quantum Dots with High Photoluminescence Quantum Yield. *J. Phys. Chem. C* **2018**, *122*, 5151−5160.

(48) Protesescu, L.; Yakunin, S.; Bodnarchuk, M. I.; Krieg, F.; Caputo, R.; Hendon, C. H.; Yang, R. X.; Walsh, A.; Kovalenko, M. V. Nanocrystals of Cesium Lead Halide Perovskites (CsPbX$_3$, X = Cl, Br, and I): Novel Optoelectronic Materials Showing Bright Emission with Wide Color Gamut. *Nano Lett.* **2015**, *15*, 3692−3696.

(49) Swarnkar, A.; Chulliyil, R.; Ravi, V. K.; Irfanullah, M.; Chowdhury, A.; Nag, A. Colloidal CsPbBr$_3$ Perovskite Nanocrystals: Luminescence Beyond Traditional Quantum Dots. *Angew. Chem.* **2015**, *127*, 15644−15648.

(50) Yakunin, S.; Protesescu, L.; Krieg, F.; Bodnarchuk, M. I.; Nedelcu, G.; Humer, M.; De Luca, G.; Fiebig, M.; Heiss, W.; Kovalenko, M. V. Low-Threshold Amplified Spontaneous Emission and Lasing from Colloidal Nanocrystals of Caesium Lead Halide Perovskites. *Nat. Commun.* **2015**, *6*, 8056.

(51) Kwak, D.-H.; Lim, D.-H.; Ra, H.-S.; Ramasamy, P.; Lee, J.-S. High performance Hybrid Graphene-CsPbBr$_{3-x}$I$_x$ Perovskite Nanocrystal Photodetector. *RSC Adv.* **2016**, *6*, 65252−65256.

(52) Hassan, Y.; Song, Y.; Pensack, R. D.; Abdelrahman, A. I.; Kobayashi, Y.; Winnik, M. A.; Scholes, G. D. Structure-Tuned Lead Halide Perovskite Nanocrystals. *Adv. Mater.* **2016**, *28*, 566−573.

(53) Huang, H.; Chen, B.; Wang, Z.; Hung, T. F.; Susha, A. S.; Zhong, H.; Rogach, A. L. Water Resistant CsPbX$_3$ Nanocrystals Coated with Polyhedral Oligomeric Silsesquioxane and Their Use as Solid State Luminophores in All-Perovskite White Light-Emitting Devices. *Chem. Sci.* **2016**, *7*, 5699−5703.

(54) Eaton, S. W.; Lai, M.; Gibson, N. A.; Wong, A. B.; Dou, L.; Ma, J.; Wang, L.-W.; Leone, S. R.; Yang, P. Lasing in Robust Cesium Lead Halide Perovskite Nanowires. *Proc. Natl. Acad. Sci. U. S. A.* **2016**, *113*, 1993−1998.

(55) Pan, J.; Quan, L. N.; Zhao, Y.; Peng, W.; Murali, B.; Sarmah, S. P.; Yuan, M.; Sinatra, L.; Alyami, N. M.; Liu, J.; Yassitepe, E.; Yang, Z.; Voznyy, O.; Comin, R.; Hedhili Mohamed, N.; Mohammed Omar, F.; Lu Zheng, H.; Kim Dong, H.; Sargent Edward, H.; Bakr Osman, M.; et al. Highly Efficient Perovskite-Quantum-Dot Light-Emitting Diodes by Surface Engineering. *Adv. Mater.* **2016**, *28*, 8718−8725.

(56) Swarnkar, A.; Marshall, A. R.; Sanehira, E. M.; Chernomordik, B. D.; Moore, D. T.; Christians, J. A.; Chakrabarti, T.; Luther, J. M. Quantum Dot−Induced Phase Stabilization of α-CCsPbI$_3$ Perovskite for High-Efficiency Photovoltaics. *Science* **2016**, *354*, 92−95.

(57) Cho, J.; Jin, H.; Sellers, D. G.; Watson, D. F.; Son, D. H.; Banerjee, S. Influence of Ligand Shell Ordering on Dimensional Confinement of Cesium Lead Bromide (CsPbBr$_3$) Perovskite Nanoplatelets. *J. Mater. Chem. C* **2017**, *5*, 8810−8818.

(58) Maes, J.; Balcaen, L.; Drijvers, E.; Zhao, Q.; De Roo, J.; Vantomme, A.; Vanhaecke, F.; Geiregat, P.; Hens, Z. Light Absorption Coefficient of CsPbBr$_3$ Perovskite Nanocrystals. *J. Phys. Chem. Lett.* **2018**, *9*, 3093−3097.

(59) Kovalenko, M. V.; Protesescu, L.; Bodnarchuk, M. I. Properties and Potential Optoelectronic Applications of Lead Halide Perovskite Nanocrystals. *Science* **2017**, *358*, 745−750.

(60) Yan, F.; Xing, J.; Xing, G.; Quan, L.; Tan, S. T.; Zhao, J.; Su, R.; Zhang, L.; Chen, S.; Zhao, Y.; Huan, A.; Sargent, E. H.; Xiong, Q.; Demir, H. V. Highly Efficient Visible Colloidal Lead-Halide Perovskite Nanocrystal Light-Emitting Diodes. *Nano Lett.* **2018**, *18*, 3157−3164.

(61) Maceiczyk, R. M.; Dümbgen, K.; Lignos, I.; Protesescu, L.; Kovalenko, M. V.; deMello, A. J. Microfluidic Reactors Provide Preparative and Mechanistic Insights into the Synthesis of Formamidinium Lead Halide Perovskite Nanocrystals. *Chem. Mater.* **2017**, *29*, 8433−8439.

(62) Dong, Y.; Qiao, T.; Kim, D.; Parobek, D.; Rossi, D.; Son, D. H. Precise Control of Quantum Confinement in Cesium Lead Halide Perovskite Quantum Dots *via* Thermodynamic Equilibrium. *Nano Lett.* **2018**, *18*, 3716−3722.

(63) Akkerman, Q. A.; Rainò, G.; Kovalenko, M. V.; Manna, L. Genesis, Challenges and Opportunities for Colloidal Lead Halide Perovskite Nanocrystals. *Nat. Mater.* **2018**, *17*, 394−405.

(64) Sanehira, E. M.; Marshall, A. R.; Christians, J. A.; Harvey, S. P.; Ciesielski, P. N.; Wheeler, L. M.; Schulz, P.; Lin, L. Y.; Beard, M. C.; Luther, J. M. Enhanced Mobility CsPbI$_3$ Quantum Dot Arrays for Record-Efficiency, High-Voltage Photovoltaic Cells. *Sci. Adv.* **2017**, *3*, eaao4204.

(65) Zou, C.; Huang, C.-Y.; Sanehira, E. M.; Luther, J. M.; Lin, L. Y. Highly Stable Cesium Lead Iodide Perovskite Quantum Dot Light-Emitting Diodes. *Nanotechnology* **2017**, *28*, 455201.

(66) Lignos, I.; Morad, V.; Shynkarenko, Y.; Bernasconi, C.; Maceiczyk, R. M.; Protesescu, L.; Bertolotti, F.; Kumar, S.;

DOI: 10.1021/acsnano.8b05555

Ochsenbein, S. T.; Masciocchi, N.; Guagliardi, A.; Shih, C.-J.; Bodnarchuk, M. I.; deMello, A. J.; Kovalenko, M. V. Exploration of Near-Infrared-Emissive Colloidal Multinary Lead Halide Perovskite Nanocrystals Using an Automated Microfluidic Platform. *ACS Nano* **2018**, *12*, 5504−5517.

(67) Wheeler, L. M.; Anderson, N. C.; Bliss, T. S.; Hautzinger, M. P.; Neale, N. R. Dynamic Evolution of 2D Layers within Perovskite Nanocrystals *via* Salt Pair Extraction and Reinsertion. *J. Phys. Chem. C* **2018**, *122*, 14029−14038.

(68) Talapin, D. V.; Haubold, S.; Rogach, A. L.; Kornowski, A.; Haase, M.; Weller, H. A Novel Organometallic Synthesis of Highly Luminescent CdTe Nanocrystals. *J. Phys. Chem. B* **2001**, *105*, 2260−2263.

(69) Norris, D. J.; Bawendi, M. G. Measurement and Assignment of the Size-Dependent Optical Spectrum in CdSe Quantum Dots. *Phys. Rev. B: Condens. Matter Mater. Phys.* **1996**, *53*, 16338−16346.

(70) Mićić, O. I.; Cheong, H. M.; Fu, H.; Zunger, A.; Sprague, J. R.; Mascarenhas, A.; Nozik, A. J. Size-Dependent Spectroscopy of InP Quantum Dots. *J. Phys. Chem. B* **1997**, *101*, 4904−4912.

(71) Ithurria, S.; Talapin, D. V. Colloidal Atomic Layer Deposition (c-ALD) using Self-Limiting Reactions at Nanocrystal Surface Coupled to Phase Transfer between Polar and Nonpolar Media. *J. Am. Chem. Soc.* **2012**, *134*, 18585−18590.

(72) Trots, D. M.; Myagkota, S. V. High-Temperature Structural Evolution of Caesium and Rubidium Triiodoplumbates. *J. Phys. Chem. Solids* **2008**, *69*, 2520−2526.

(73) Stoumpos, C. C.; Kanatzidis, M. G. The Renaissance of Halide Perovskites and Their Evolution as Emerging Semiconductors. *Acc. Chem. Res.* **2015**, *48*, 2791−2802.

(74) Weller, M. T.; Weber, O. J.; Frost, J. M.; Walsh, A. Cubic Perovskite Structure of Black Formamidinium Lead Iodide, α-$[HC(NH_2)_2]PbI_3$, at 298 K. *J. Phys. Chem. Lett.* **2015**, *6*, 3209−3212.

(75) Fabini, D. H.; Stoumpos, C. C.; Laurita, G.; Kaltzoglou, A.; Kontos, A. G.; Falaras, P.; Kanatzidis, M. G.; Seshadri, R. Reentrant Structural and Optical Properties and Large Positive Thermal Expansion in Perovskite Formamidinium Lead Iodide. *Angew. Chem., Int. Ed.* **2016**, *55*, 15392−15396.

(76) Weber, O. J.; Ghosh, D.; Gaines, S.; Henry, P. F.; Walker, A. B.; Islam, M. S.; Weller, M. T. Phase Behavior and Polymorphism of Formamidinium Lead Iodide. *Chem. Mater.* **2018**, *30*, 3768−3778.

(77) De Roo, J.; Ibáñez, M.; Geiregat, P.; Nedelcu, G.; Walravens, W.; Maes, J.; Martins, J. C.; Van Driessche, I.; Kovalenko, M. V.; Hens, Z. Highly Dynamic Ligand Binding and Light Absorption Coefficient of Cesium Lead Bromide Perovskite Nanocrystals. *ACS Nano* **2016**, *10*, 2071−2081.

(78) Zhu, X.; Su, H.; Marcus, R. A.; Michel-Beyerle, M. E. Computed and Experimental Absorption Spectra of the Perovskite $CH_3NH_3PbI_3$. *J. Phys. Chem. Lett.* **2014**, *5*, 3061−3065.

(79) Endres, J.; Egger, D. A.; Kulbak, M.; Kerner, R. A.; Zhao, L.; Silver, S. H.; Hodes, G.; Rand, B. P.; Cahen, D.; Kronik, L.; Kahn, A. Valence and Conduction Band Densities of States of Metal Halide Perovskites: A Combined Experimental−Theoretical Study. *J. Phys. Chem. Lett.* **2016**, *7*, 2722−2729.

(80) Ravi, V. K.; Markad, G. B.; Nag, A. Band Edge Energies and Excitonic Transition Probabilities of Colloidal $CsPbX_3$ (X = Cl, Br, I) Perovskite Nanocrystals. *ACS Energy Lett.* **2016**, *1*, 665−671.

(81) Amat, A.; Mosconi, E.; Ronca, E.; Quarti, C.; Umari, P.; Nazeeruddin, M. K.; Grätzel, M.; De Angelis, F. Cation-Induced Band-Gap Tuning in Organohalide Perovskites: Interplay of Spin−Orbit Coupling and Octahedra Tilting. *Nano Lett.* **2014**, *14*, 3608−3616.

(82) Haruyama, J.; Sodeyama, K.; Han, L.; Tateyama, Y. First-Principles Study of Ion Diffusion in Perovskite Solar Cell Sensitizers. *J. Am. Chem. Soc.* **2015**, *137*, 10048−10051.

(83) Pan, D.; Fu, Y.; Chen, J.; Czech, K. J.; Wright, J. C.; Jin, S. Visualization and Studies of Ion-Diffusion Kinetics in Cesium Lead Bromide Perovskite Nanowires. *Nano Lett.* **2018**, *18*, 1807−1813.

(84) Wang, Q.; Jin, Z.; Chen, D.; Bai, D.; Bian, H.; Sun, J.; Zhu, G.; Wang, G.; Liu, S. μ-Graphene Crosslinked $CsPbI_3$ Quantum Dots for High Efficiency Solar Cells with Much Improved Stability. *Adv. Energy Mater.* **2018**, *8*, 1800007.

(85) Wheeler, L. M.; Sanehira, E. M.; Marshall, A. R.; Schulz, P.; Suri, M.; Anderson, N. C.; Christians, J. A.; Nordlund, D.; Sokaras, D.; Kroll, T.; Harvey, S. P.; Berry, J. J.; Lin, L. Y.; Luther, J. M. Targeted Ligand-Exchange Chemistry on Cesium Lead Halide Perovskite Quantum Dots for High-Efficiency Photovoltaics. *J. Am. Chem. Soc.* **2018**, *140*, 10504−10513.

(86) Caraballo, F.; Kumano, M.; Saeki, A. Spatial Inhomogeneity of Methylammonium Lead-Mixed Halide Perovskite Examined by Space- and Time-Resolved Microwave Conductivity. *ACS Omega* **2017**, *2*, 8020−8026.

(87) Shockley, W.; Queisser, H. J. Detailed Balance Limit of Efficiency of p-n Junction Solar Cells. *J. Appl. Phys.* **1961**, *32*, 510−519.

(88) Shannon, R. D. Revised Effective Ionic Radii and Systematic Studies of Interatomic Distances in Halides and Chalcogenides. *Acta Crystallogr., Sect. A: Cryst. Phys., Diffr., Theor. Gen. Crystallogr.* **1976**, *32*, 751−767.

(89) Kieslich, G.; Sun, S.; Cheetham, A. K. An Extended Tolerance Factor Approach for Organic-Inorganic Perovskites. *Chem. Sci.* **2015**, *6*, 3430−3433.

(90) Rühle, S. Tabulated Values of the Shockley−Queisser Limit for Single Junction Solar Cells. *Sol. Energy* **2016**, *130*, 139−147.

DOI: 10.1021/acsnano.8b05555